

# Oxygen-Driven Metal–Insulator Transition in SrNbO<sub>3</sub> Thin Films Probed by Infrared Spectroscopy

Paola Di Pietro, Chiara Bigi, Sandeep Kumar Chaluvadi, Daniel Knez, Piu Rajak, Regina Ciancio, Jun Fujii, Francesco Mercuri, Stefano Lupi, Giorgio Rossi, Francesco Borgatti, Andrea Perucchi, and Pasquale Orgiani\*

The occurrence of oxygen-driven metal–insulator-transition (MIT) in SrNbO<sub>3</sub> (SNO) thin films epitaxially grown on (110)-oriented DyScO<sub>3</sub> has been reported. SNO films are fabricated by the pulsed laser deposition technique at different partial O<sub>2</sub> pressure to vary the oxygen content and their structural, optical, and transport properties are probed. SNO unit cell has been found to shrink vertically as the oxygen content increases but keeping the epitaxial matching with the substrate. The results of Fourier-transform infra-red spectroscopy show that highly oxygenated SNO samples (i.e., grown at high oxygen pressure) show distinct optical conductivity behavior with respect to oxygen deficient films, hence demonstrating the insulating character of the formers with respect to those fabricated with lower pressure conditions. Tailoring the optical absorption and conductivity of strontium niobate epitaxial films across the MIT will favor novel applications of this material.

addition to this strategy, the electronic and magnetic properties of these oxides, as well as the performance of devices based on their use, are also extremely sensitive to the oxygen content in the lattice. For example, oxygen vacancies acting as shallow donors can drastically affect the number of conducting electrons and have a significant role in the catalytic properties of perovskites,<sup>[4]</sup> while p-doping through hosting excess oxygen ions in the lattice was demonstrated as an effective way to modulate the band-filling of 3d valence states,<sup>[5]</sup> and bias-induced drifting of oxygen ions in/out of the perovskite modifies significantly the resistance of memristive devices in the boundary region among the oxide and the metal electrode.<sup>[6,7]</sup>

## 1. Introduction

The class of perovskite oxides with general composition ABO<sub>3</sub>, in which A are either rare-earth or alkali-earth cations, B are transition metal ions and the anion is oxygen, is attracting more and more interest due to the wide spread of technologically important phenomena which can be displayed.<sup>[1,2]</sup> Regarding energy applications, they can be used as catalysts, as high-performance cathode in various solid oxide fuel cell devices, as electrolyte materials for proton conductors and many others. Chemical doping of perovskites through cation substitution is an established strategy to tailor the functionalities of these compounds.<sup>[3]</sup> However, in

At variance with the most explored 3d compounds, for the isostructural perovskites hosting 4d transition metal ions the more extended 4d electronic states in the B-site provide larger hybridization with the surrounding oxygen ions and weaker on-site Coulomb repulsion, thus promoting stronger metallic behavior and reduced electronic correlation effects. In particular, strontium niobate SrNbO<sub>3</sub> (SNO, Nb 4d<sup>1</sup> nominal valence) has recently attracted a lot of interest as a promising visible-light photocatalysts for water splitting,<sup>[8–10]</sup> and as a transparent conductor in the visible and ultraviolet spectra, which makes it an ideal electrode material for high-performance UV light emitting diodes and for plasmonics.<sup>[11–13]</sup> Moreover,

P. Di Pietro, A. Perucchi  
 Elettra Sincrotrone Trieste S.C.p.A.  
 Trieste I-34139, Italy

C. Bigi, S. K. Chaluvadi, D. Knez, P. Rajak, R. Ciancio, J. Fujii, S. Lupi, G. Rossi, P. Orgiani  
 CNR-IOM TASC Laboratory  
 Area Science Park  
 Trieste I-34149, Italy  
 E-mail: pasquale.orgiani@cnr.it

F. Mercuri, F. Borgatti  
 Istituto per lo Studio dei Materiali Nanostrutturati  
 Consiglio Nazionale delle Ricerche (CNR-ISMN)  
 Bologna Division  
 Bologna I-40129, Italy

S. Lupi  
 Department of Physics  
 University of Roma La Sapienza  
 Roma I-00185, Italy

C. Bigi, G. Rossi  
 Department of Physics  
 University of Milano  
 Milano I-20133, Italy

 The ORCID identification number(s) for the author(s) of this article can be found under <https://doi.org/10.1002/aelm.202101338>.

© 2022 The Authors. Advanced Electronic Materials published by Wiley-VCH GmbH. This is an open access article under the terms of the Creative Commons Attribution License, which permits use, distribution and reproduction in any medium, provided the original work is properly cited.

DOI: 10.1002/aelm.202101338

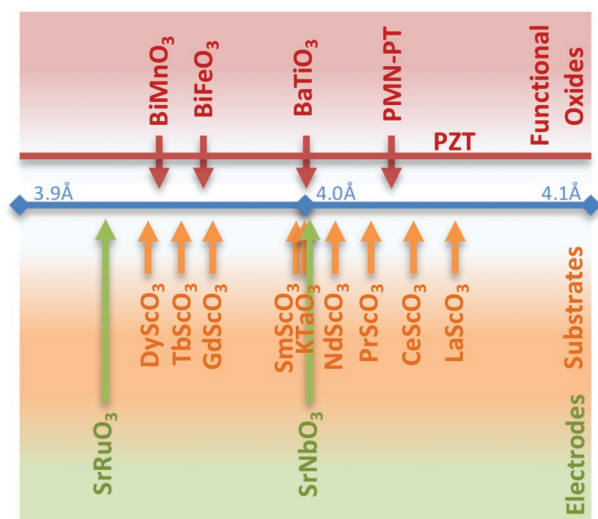


**Figure 1.** A number of the pseudotetragonal or pseudocubic  $a$ -axis lattice constants of some perovskite functional oxides and substrates that are available commercially; below, the  $a$ -axis lattice parameters of SrRuO<sub>3</sub> and SrNbO<sub>3</sub> - materials for potential electrodes - are also reported.

while recent progresses in the synthesis of rare-earth scandiate oxide single-crystals allow the coherent growth of functional perovskites (e.g., ferroelectrics, multiferroics) characterized by large lattice parameters,<sup>[14]</sup> the choice of the material for electrodes is mostly confined to the strontium ruthenate SrRuO<sub>3</sub>, whose electrical properties, however, are strongly dependent on substrate induced strain mechanism.<sup>[15,16]</sup> On the contrary, the large in-plane lattice parameters of SNO indicate it as an ideal candidate for multi-layered epitaxial heterostructures (**Figure 1**). The electronic band structure of oxygen-deficient SNO thin films was recently probed by angle-resolved photoelectron spectroscopy (ARPES).<sup>[17]</sup> SNO films were grown over several substrates and conditions, showing a strong sensitivity to the fabrication conditions.<sup>[18,19]</sup> Yet, a key point in optimizing the functionalities of this material, as well as discovering new ones, is determining the strict correlation between the structural and electronic properties.

In this work, we report on the dependence on the oxygen content of fully strained epitaxial SNO thin films ( $\approx 15$  nm) grown on (110)-oriented DyScO<sub>3</sub> (DSO) substrates<sup>[14]</sup> by pulsed laser deposition (PLD). The oxygen content of the films was tuned in the deposition process by fixing the background oxygen pressure  $P_{\text{PLD}}(\text{O}_2)$  in the PLD system. The structural characterization by X-ray diffraction (XRD), X-ray reflectivity (XRR), and high-resolution transmission electron microscopy (HR-TEM) ensures the quality of the SNO films for the whole range of  $P_{\text{PLD}}(\text{O}_2)$ . Since the in-plane atomic arrangement is constrained by the epitaxial matching with the underlying lattice registry of the substrate,<sup>[20–22]</sup> the influence of the oxygen content on the properties of the SNO films can be determined independently of other structural effects,<sup>[23]</sup> Fourier-transform infrared (FTIR) spectroscopy measurements highlight the occurrence of a metal-to-insulator transition (MIT) governed by varying the oxygen pressure during the growth of the films. The optical conductivity obtained from the FTIR results make

this behavior remarkably evident, consistently with previous optical studies performed in the visible/UV energy range,<sup>[9,10]</sup> that the highly oxygenated films are strongly insulating, while those fabricated with low oxygen pressure are largely conductive. The large sensitivity of the SNO films to the modulation of the oxygen content through the fabrication conditions opens the perspective for novel applications exploiting the oxygen-driven MIT of this material, for example, as resistive-switching random-access-memories (RRAMs) in which the switching behavior can be manipulated controlling the oxygen content during the fabrication.<sup>[24]</sup>

## 2. Structural Characterization

The bulk of single crystal SNO has an orthorhombic crystal structure (space group Pnma) with lattice constants of  $a = 0.569$  nm,  $b = 0.570$  nm, and  $c = 0.807$  nm.<sup>[18]</sup> Yet, a pseudo-cubic subunit cell with lattice constants  $a \approx 0.4023$  nm is usually adopted in which, as other members of the perovskite oxides family,<sup>[20,21]</sup> the Sr stays at its center and the Nb-ions at its corner, the latter octahedrally coordinated with the surrounding first-neighbor oxygen ions. Similarly, DyScO<sub>3</sub> has an orthorhombic structure (space group Pbnm) with lattice constants of  $a = 0.54494$  nm,  $b = 0.57263$  nm, and  $c = 0.79132$  nm and a pseudo-cubic sub-unit cell along the (110) direction with lattice constants of about 0.396 nm. Compared to the growth of SNO films on other substrates such as LaAlO<sub>3</sub> and SrTiO<sub>3</sub>,<sup>[9,10,19]</sup> for which a partial strain relaxation was observed, coherent growth is favored by the smaller misfit with the DSO substrate (i.e.,  $-1.5\%$ ), similarly to the case of high-quality SNO films grown on KTaO<sub>3</sub>(001).<sup>[11]</sup> Since obtaining the SNO compound with the perovskite structure is quite difficult,<sup>[18,19]</sup> we have performed a detailed structural characterization in order to identify the phase, the crystalline quality, and the epitaxial relationship for the SNO films deposited on DyScO<sub>3</sub>(110) varying the oxygen pressure  $P_{\text{PLD}}(\text{O}_2)$  in the PLD system from  $10^{-2}$  to  $10^{-4}$  mbar. It turns out that the SNO films are epitaxially grown on DSO substrates for any deposition oxygen pressure. The SNO in-plane lattice registry fully matches the DSO substrate, while the SNO out-of-plane lattice parameters evolves with the oxygen content toward a progressive increase of the  $c/a$  ratio of the pseudo-cubic unit cell.

In particular, in **Figure 2a**, we show the main results of HRTEM characterization of a SNO film fabricated with  $P_{\text{PLD}}(\text{O}_2) = 10^{-4}$  mbar. In **Figure 2** panel (a), the HRTEM bright-field cross-sectional image of the film highlights an abrupt, high-quality, epitaxial interface with the underlying DSO substrate. The structure of the film over the whole image is homogeneous, and free of significant defects. No structural differences were detected among the near-interface region and the bulk of the film, as well as no traces of spurious phases or segregation of crystalline phases other than SNO. The phase-contrast variations in the SNO-region are common features in HRTEM image and they can be a result of specimen preparation. The panels on the right show fast Fourier transformation (FFT) patterns calculated from the corresponding highlighted regions in film and substrate, respectively. The diffractogram of SNO can be safely assigned to a pseudo-cubic perovskite structure. The

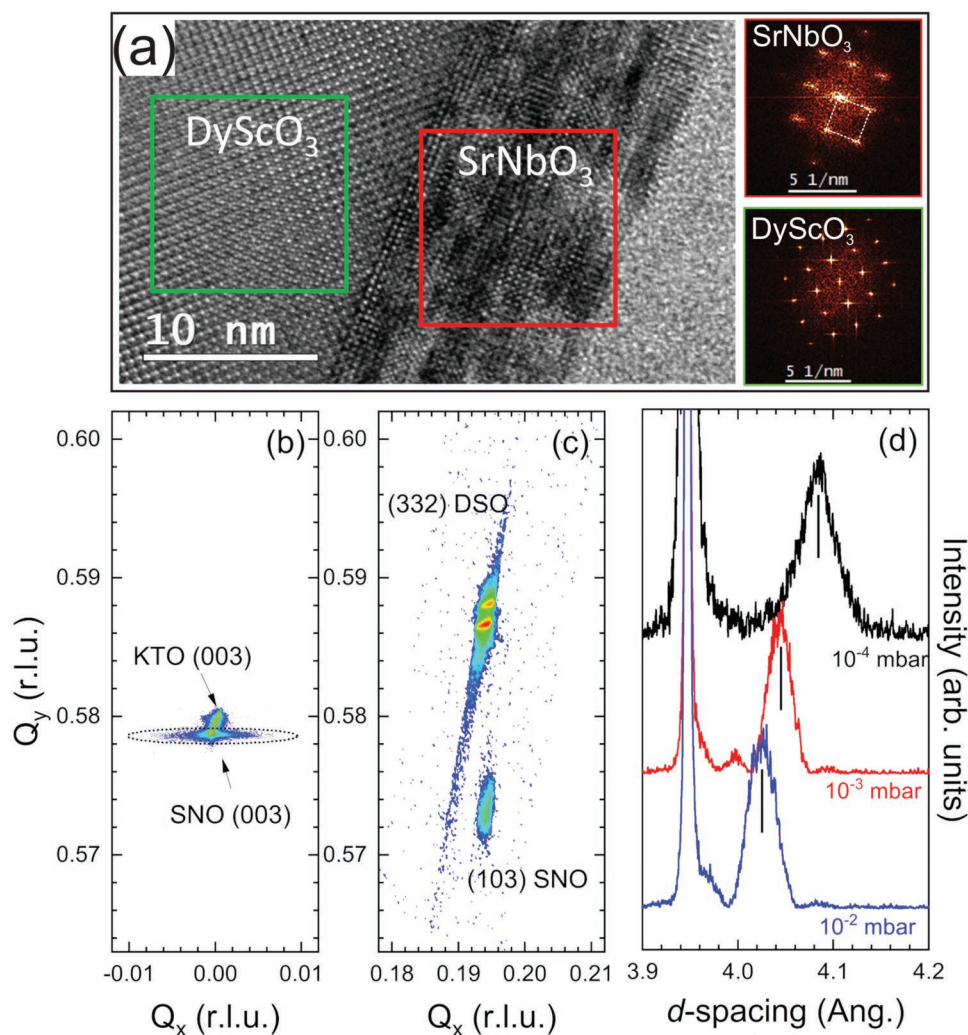


**Figure 2.** a) Cross-sectional HRTEM image for a SNO film grown on DSO substrate with  $P_{\text{PLD}}(\text{O}_2) = 10^{-4}$  mbar. On the right, FFT patterns for selected area of the the SNO film (red box, top) and the DSO substrate (green box, bottom), respectively. The regions from which the FFTs were calculated are indicated in the HRTEM image. b) Reciprocal space map around the (003) SNO symmetric Bragg reflection of a SNO strainless film grown on KTO substrate. c) Representative reciprocal space map around the (103) SNO asymmetric Bragg reflection. d) Evolution of the out-of-plane lattice cell for SNO films grown under oxygen pressure ranging from  $10^{-2}$  to  $10^{-4}$  mbar. The  $d$ -spacing values were extracted from the (002) symmetric Bragg reflections.

absence of superstructure reflections indicates that the SNO lattice does not adopt an orthorhombically distorted structure.

In order to disentangle the out-of-plane and the in-plane structural properties of the SNO films, the crystal structure was probed by XRD, mapping the reciprocal space region around symmetrical and asymmetrical Bragg reflections. Figure 2c shows the map of the (103) asymmetric Bragg reflection for a film grown at the lowest oxygen pressure. The map was measured after the alignment of the substrate crystallographic planes and reported in reciprocal lattice units (r.l.u.). It is worth to notice that the SNO and DSO diffraction peaks are very well aligned along the  $Q_x$  direction, thus proving in-plane matching of the lattice parameters. The mismatch among the surface cells of SNO and DSO is about  $-1.5\%$ , thus epitaxial growth of the films implies in-plane compressive strain of the SNO cell. As a consequence, SNO diffraction peak shifts to lower  $Q_y$ - values with respect to the strainless-condition measured in

SNO films grown on  $\text{KTaO}_3$  (KTO) substrates (Figure 2b). We obtained similar results for all the investigated samples, independently of the oxygen growth pressure, hence the depositing pressure  $P_{\text{PLD}}(\text{O}_2)$  has little influence on the structural quality of the SNO films.

The different values of the out-of-plane lattice constant obtained from the position of the (002) symmetric Bragg reflections, shown in Figure 2d, shows a progressive increment from 0.402 nm for the highly oxygenated (i.e.,  $P_{\text{PLD}}(\text{O}_2) = 10^{-2}$  mbar) to 0.409 nm for the oxygen deficient (i.e.,  $P_{\text{PLD}}(\text{O}_2) = 10^{-4}$  mbar) sample. Reducing  $P_{\text{PLD}}(\text{O}_2)$  thus promotes a slight tetragonal distortion of the SNO pseudo-cubic unit cell characterized by the ratio  $c/a$ , where  $a$  is the in-plane lattice constant, which varies from 1.016 to 1.033. The elastic deformation of the unit cell, calculated on the basis of the elastic constants of SNO<sup>[25,26]</sup> cannot account by itself for the large expansion of the films grown at  $P_{\text{PLD}}(\text{O}_2) = 10^{-4}$  mbar, indicating that the

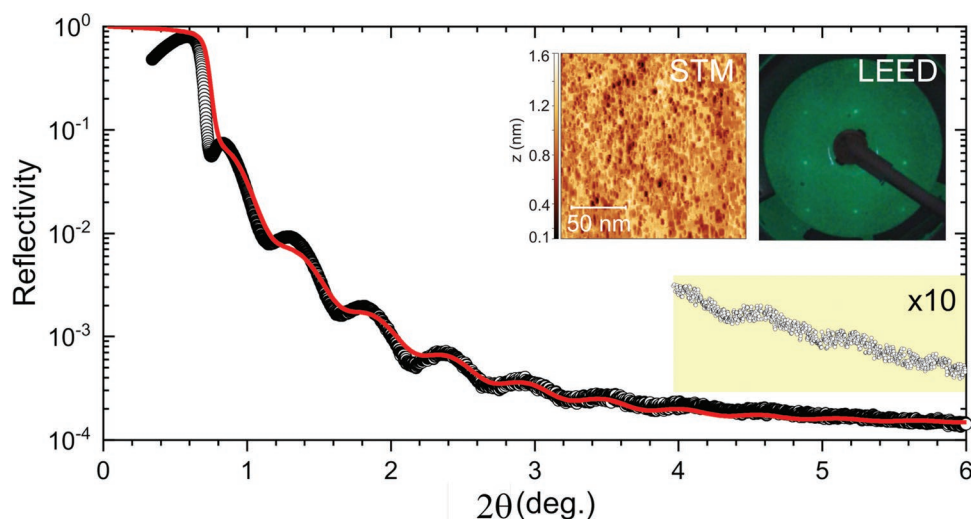


**Figure 3.** X-ray reflectivity (black symbols) of 15-nm-thick SNO film grown on DSO substrate and the correspondent fitting curve (red line). The oscillatory behavior of the XRR scan at high incident angles is vertically expanded for clarity. Inset panels: (left) typical STM topography image and (right) LEED pattern of the SNO surface obtained for  $\approx 50$  eV electron kinetic energy. The root-mean-square (RMS) roughness from the STM image is  $\approx 0.2$  nm, consistent with the RMS value obtained from the XRR analysis.

progressive out-of-plane elongation of the unit cell is likely favored by the presence of oxygen vacancies. As it has been observed even for other perovskites, these vacancies stabilize the epitaxial growth of the films through increasing the out-of-plane lattice parameter while the in-plane matching with the substrate is preserved.<sup>[22,27–29]</sup> This indication is supported by recent core-level photo-electron spectroscopy measurements of SNO films fabricated on DSO with  $P_{\text{PLD}}(\text{O}_2) = 10^{-4}$  mbar.<sup>[17]</sup> In particular, the full-width at half maximum (FWHM) of diffraction peak looks to slightly increase in the sample grown at lower oxygen pressure, resulting in an increase value of statistical error on the determination of the out-of-plane lattice parameter (i.e., 0.004 and 0.003 nm for samples grown at  $10^{-4}$  mbar and  $10^{-3}/10^{-2}$  mbar, respectively). This might be likely due to the increase of the structural disorder promoted by the increment of randomly distributed oxygen vacancies in the film, however a small increase of the FWHM also occurs in the diffraction peak of the substrate, thus suggesting a correlation between these two features. Since the FWHM of the diffraction peaks does not substantially vary among all of the investigated samples, we do not expect that those differences might affect significantly the optical properties.

Since both surface roughness and morphology are significant in perspective of technological applications, for example, involving the fabrication of layered heterostructures, we have also performed XRR measurements. The XRR curve for epitaxial SNO films with thickness of about 15 nm is shown in **Figure 3** with the fitting curve obtained by the IMD package of the XOP software.<sup>[30,31]</sup> Even though the XRR fitting algorithm is based on a monochromatized X-ray source with negligible lateral inhomogeneities of the beam (while we used a lab-based unmonochromatized X-ray beam), the surface root-mean-square (RMS) roughness was estimated to be  $\approx 0.4$  nm, corresponding to about one single SNO unit cell. Yet such a value must be considered as an upper limit for the surface RMS. As a matter of fact, the actual surface of the SNO films was specifically

probed by in situ scanning tunnel microscopy (STM). The STM measurements, shown in the inset (left), indicate a very smooth surface with typical RMS roughness  $< 0.2$  nm, corresponding to less than half of the pseudocubic unit cell. Such a value is consistent with the RMS obtained from the XRR analysis performed on millimeter-scale. The LEED pattern, sensitive to the ordering of the surface layers, shows a simple cubic pattern without extra spots, indicating that no surface reconstruction occurs. The occurrence of atomically flat surfaces and the absence of spurious extra phases make these films as ideal candidates to investigate the intrinsic physical properties of SNO as a function of a single parameter that is, the oxygen content.

### 3. Infrared Spectroscopy

The dependence of the low-energy electro-dynamics of the SNO films on the oxygen pressure has been investigated by infrared FTIR spectroscopy, focusing in particular on the intra-band transitions across the Fermi energy. **Figure 4a** shows the room-temperature reflectivity of the SNO films as a function of the photon energy  $\hbar\omega$ . The photon energy range is 0.009–1 eV, correspondent to  $\approx 70$ –8000  $\text{cm}^{-1}$ . The spectra are shown on logarithmic energy scale to highlight the far-infrared region (FIR,  $\hbar\omega \leq 0.1$  eV) exhibiting peaks attributed to infrared (IR) active phonon modes, and the progressive disappearing of the local minimum at about 0.09 eV which is totally absent in the spectrum for the lowest pressure. The reflectivity of the DSO bare substrate in the far-IR spectral region is reported in the inset as a reference. It is worth to notice that the clear, monotonic increase of the overall reflectivity as  $P_{\text{PLD}}(\text{O}_2)$  is progressively reduced is indicative of larger metallicity of the samples, therefore the corresponding reduction of the phonon peaks is associated to the more effective screening provided by the larger free-carrier contribution.

The optical constants and the conductivity of the SNO films were obtained through fitting the FTIR measurements with the

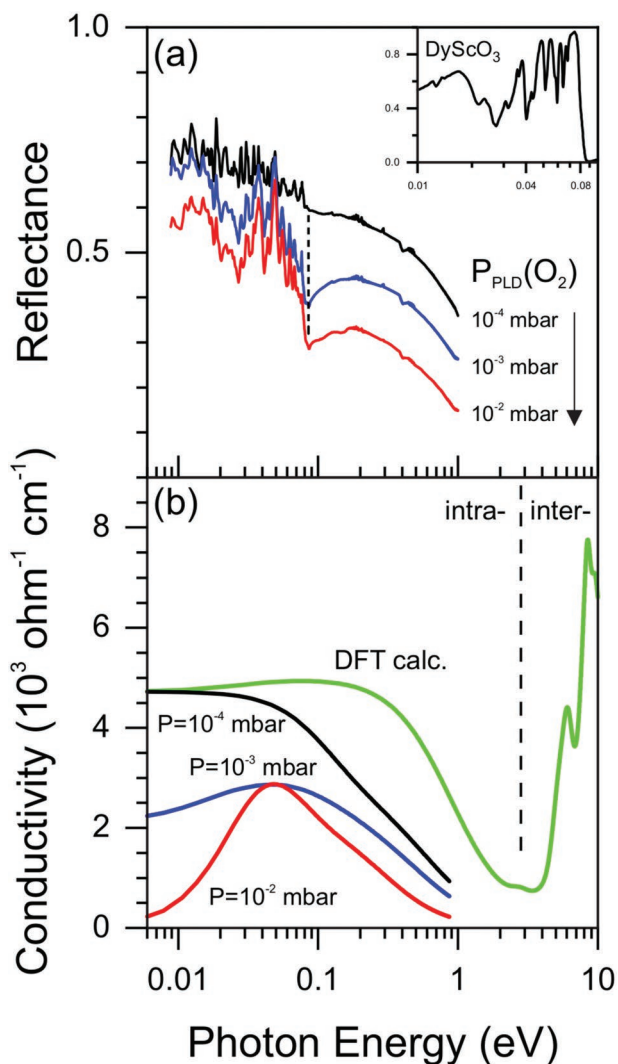


**Figure 4.** a) Reflectivity of SNO thin films grown on DSO substrate with different oxygen growth pressure. The phonon modes occurs in the FIR region below 0.1 eV (vertical shaded line). The increase of the overall reflectivity indicates larger metallic character for the films grown at lower oxygen pressure. Inset: reflectivity of the bare substrate. Inset: reflectivity of the bare substrate in the far-IR spectral region. b) Real part  $\sigma_1(\omega)$  of the conductivity for the SNO films, as obtained from the analysis of the reflectivity spectra. The intensity varies with the oxygen growth pressure consistently with the reflectivity results. The DFT calculation of  $\sigma_1(\omega)$  for stoichiometric epitaxial SNO film (dashed line) supports for the larger metallicity of the film grown at the lowest oxygen pressure.

ReFIT software.<sup>[32]</sup> The reflectivity of the samples together with the substrate is fitted by using a two-layers Kramers–Krönig consistent Drude–Lorentz (DL) model in which the relative permittivity of each material as a function of the photon energy is given by

$$\epsilon_{\text{DL}}(\omega) = \epsilon_{\infty} + \sum_{j=1}^N \frac{A_j^2}{\omega^2 - \omega_{0,j}^2 + i\Gamma_j\omega} \quad (1)$$

where  $N$  is the number of Drude–Lorentz terms,  $\epsilon_{\infty}$  is the contribution of inter-band transitions beyond the energy range

being considered,  $A_j$  is the amplitude of the  $j$ -th mode,  $\omega_{0,j}$  is the resonance frequency, and  $\Gamma_j$  is the damping coefficient. The free electrons are described by Drude term with  $\omega_{0,j} = 0$ . This model accounts for both intra-band (free electrons) and inter-band (bound electrons) excitations. The optical conductivity is then obtained through the relationship

$$\epsilon(\omega) = \epsilon_0 + \frac{i\sigma(\omega)}{\omega} \quad (2)$$

where  $\epsilon_0$  is the vacuum permittivity. The values of the DL parameters are summarized in **Table 1** and will be discussed subsequently. The extracted real part  $\sigma_1(\omega)$  of the conductivity is shown in Figure 4b, where the logarithmic energy scale is maintained for consistency with panel (a), although the energy range is slightly larger in order to favor the comparison among experiment and theory. Since the Lorentzian parameters for the phononic excitations were entirely consistent with the spectral contributions by the DSO substrate (inset of panel (a)),<sup>[33]</sup> the  $\sigma_1(\omega)$  experimental curves of the SNO films do not show any contribution related to the peaks appearing in the FIR region. The absence of significant contributions by SNO has been attributed to the small thickness of the films, which makes their contribution negligible with respect to the substrate. Noticeably, the optical conductivity shows a marked change in the energy region  $\hbar\omega \leq 0.1$  eV. In metallic systems, this region is occupied by the Drude contribution of the free charges. For increasing  $P_{\text{PLD}}(\text{O}_2)$ , the progressive reduction of the conductivity in the Drude region is accompanied by an overall decay, and shifting of the maximum conductivity to higher energy up to  $\approx 0.04$  eV. This behavior is a clear indication of metal-to-insulator transition (MIT) governed by the growth conditions. The straightforward evidence of this oxygen-driven metal–insulator transition is remarkable, and it is fully consistent with the optical spectroscopy results performed in the UV–vis energy range by Wang et al.<sup>[9,10]</sup>

The  $\sigma_1(\omega)$  curves are compared to the optical conductivity calculated by density functional theory (DFT) for stoichiometric SNO with the lattice parameters of the film fabricated with the lowest oxygen pressure. The closeness of the theoretical and experimental conductivity values at  $\hbar\omega = 0$  eV is not strictly significant, since the former is largely influenced by the choice of some parameters, such as the Lorentzian broadenings. This calculation does not take into account the presence of oxygen vacancies, however it is largely consistent with the optical conductivity of this film, in agreement with the metallic character of stoichiometric SNO. In particular, the significant intensity in the low-energy region of the calculation is associated to a Drude-like contribution by free charge carriers, while the minimum at about 2–3 eV corresponds to the passage from the intra-band to the inter-band electronic transitions, provided by previous DFT studies, reporting the partial occupancy of Nb 4d conduction states below the Fermi level.<sup>[9,10,12]</sup>

In order to better investigate this oxygen-driven metal-to-insulator transition, the DL contributions obtained from the fitting analysis of the FTIR measurements have been singled out in the optical conductivity, as shown in **Figure 5**. SNO films grown under higher oxygen pressure are clearly insulating, as the low-frequency contribution to the optical conductivity is

**Table 1.** Drude–Lorentz fit parameters. All the symbols refer to Equation (1).  $\omega_p$  here is the plasma frequency of the samples. The  $\omega_p$  values are used in Equation (4), that is,  $A_j = \text{Drude}$  in Equation (1).

Parameters [eV]	$P_{\text{PLD}}(\text{O}_2)$ [mbar]		
	$10^{-4}$	$10^{-3}$	$10^{-2}$
$\epsilon_\infty$	5.6	4	3.0
$\omega_{0, \text{Drude}}$	0.0	0.0	–
$\omega_p$	1.91	1.12	–
$\Gamma_{\text{Drude}}$	0.10	0.08	–
$\omega_{0, \text{FIR}}$	–	0.06	0.04
$A_{\text{FIR}}$	–	0.12	1.34
$\Gamma_{\text{FIR}}$	–	0.28	0.09
$\omega_{0, \text{MIR}}$	0.24	0.20	0.19
$A_{\text{MIR}}$	3.22	2.60	1.74
$\Gamma_{\text{MIR}}$	0.76	0.70	0.41

almost negligible, then the increase of the conductivity in the low energy region for decreasing pressure implies the appearance of a Drude contribution which becomes dominant for the lowest growth pressure. The behavior of the DL contributions reflects the progressive transition from insulating to metallic state. In the most insulating sample two components are present, one (“F”) centered around 0.04 eV ( $\approx 320 \text{ cm}^{-1}$ ) and the other (“M”) centered around 0.19 eV ( $\approx 1500 \text{ cm}^{-1}$ ), namely a FIR band and a MIR band, respectively. For the most conductive sample still two components occur, but the F term is replaced by the Drude (“D”) term related to the presence of free charges, while the M contribution is slightly shifted at higher energy around 0.24 eV ( $\approx 1900 \text{ cm}^{-1}$ ). All these spectral components are present for films grown at  $P_{\text{PLD}}(\text{O}_2) = 10^{-3}$  mbar, hence showing the existence of an intermediate condition likely due to coexisting conductive/insulating phases. This behavior is consistent with the structural information suggesting that the passage to the insulating phase of SNO occurs progressively through fine tuning of the oxygen content in the lattice.

The spectral weight (SW) of the D, F, and M contributions to the optical conductivity is shown in **Figure 6a**. The SW is defined as the area underneath the optical conductivity, that is

$$\text{SW}_j(\Omega, T = 300 \text{ K}) = \int_0^\Omega \sigma_{1,j}(\omega, T = 300 \text{ K}) d\omega \quad (3)$$

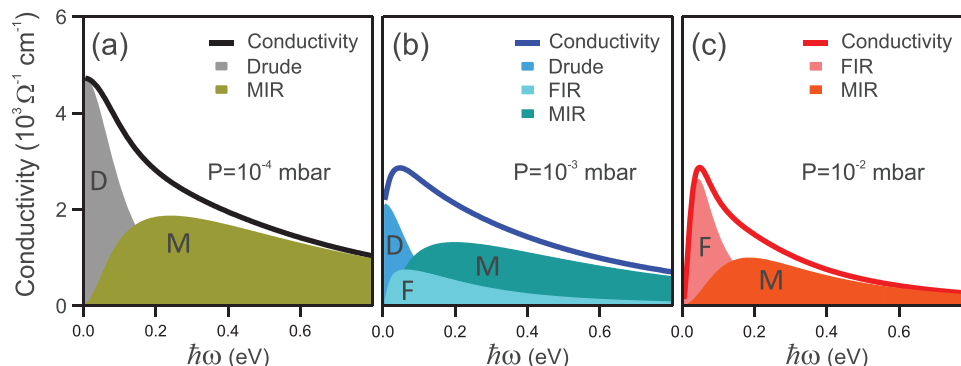


**Figure 5.** Drude–Lorentz components of the optical conductivity of all the SNO samples.

where  $j = \text{D, F, M}$ , and  $\Omega$  is a frequency cut-off corresponding to a minimum in the optical conductivity. This value counts only the contribution of the carriers due to intra-band transitions. All the SWs show a clear dependence on the oxygen growth pressure. However, while the M term is monotonically reduced for increasing pressure, the D and F terms look inversely correlated, with the former being progressively replaced by the latter. The strength of the D and F SWs is therefore a direct indicator of the metallic/insulating character of the films.

In absence of specific calculations, we identify the origin of these contributions on the basis of a phenomenological picture in which the conductive SNO films are seen as “doped” by oxygen vacancies (ions) during the growth at low (high) pressure. Indeed, when the  $\text{O}_2$  amount in the film increases, the number of  $\text{O}_2$  vacancies decreases, and the free-electrons contribution (Drude) leaves the space to a band centered at a finite frequency (F band) due to the formation of localized states. In this case, the correlation effects increase and the material becomes more insulating.<sup>[17]</sup> In particular, for the highest oxygen pressure during the growth ( $10^{-2}$  mbar) the material is an insulator and the Drude term completely disappears, while the F band becomes more intense. On the other hand the M term, whose spectral weight decreases progressively for increasing pressure, can be assigned to an absorption band related to impurities, such as the oxygen vacancies or other defects, as also reported for oxide materials like  $\text{TiO}_2$  and  $\text{LaNiO}_3$ , or to the incoherent part of the Drude term.<sup>[27,34–37]</sup>

Since the Drude term of the optical conductivity is related to the DC value by the formula

$$\sigma_{\text{DC,optical}} = \frac{\omega_p^2}{4\pi\Gamma_{\text{Drude}}} \quad (4)$$

where  $\omega_p$  is the plasma frequency and  $\Gamma_{\text{Drude}}$  is the Drude scattering rate, both extracted from the D–L fitting procedure (see Table 1), the DC conductivity has been also calculated. As reported in Figure 6b, those values agree very well with those extracted by transport measurements, indicating that the optical spectroscopy reliably allows to account for the overall conductive behavior of the samples. The agreement between the values extracted from transport and optical measurements indicates that the most relevant contribution to the electron density mainly comes from the free carrier contribution.

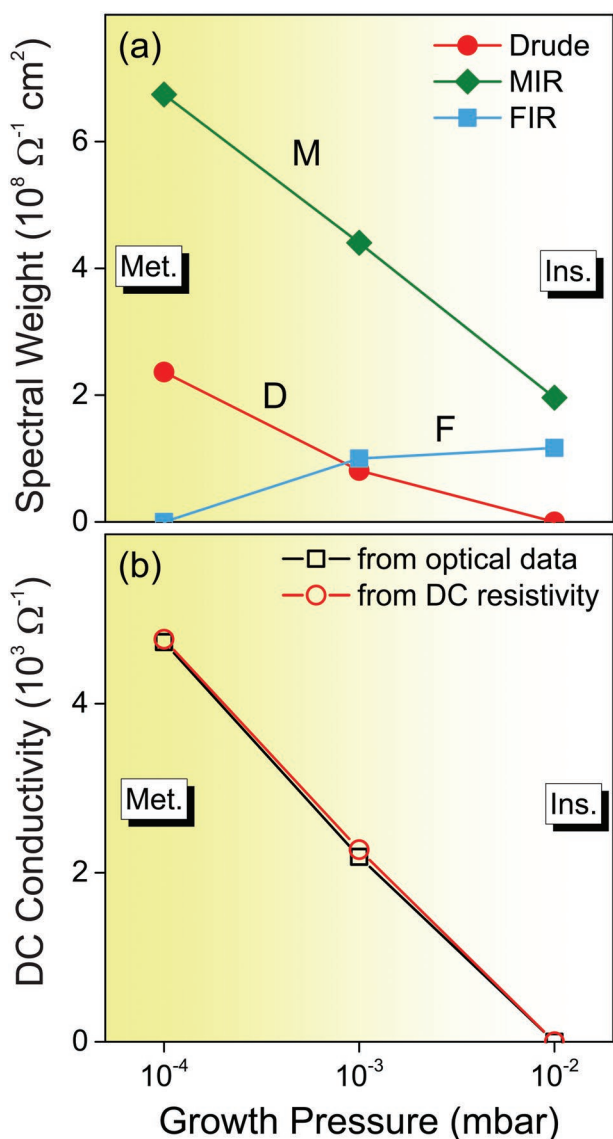


**Figure 6.** a) Dependence of the spectral weights in the optical conductivity on the oxygen pressure during the film growth. The parameters of these terms are reported in Table 1. The MIR term exhibits a monotonic behavior, while spectral weight of the D and F terms is inversely correlated. b) Comparison of the DC conductivity measured by optics and transport.

Finally, the optical conductivity allows to calculate also the carrier density of the samples. The effective number of carriers contributing to electromagnetic absorption at frequencies below  $\Omega$  can be calculated by the formula:

$$N_{\text{eff}}(\Omega, T = 300 \text{ K}) = \frac{2m_e}{\pi e^2} \text{SW}(\Omega, T = 300 \text{ K}) \quad (5)$$

where  $e$  and  $m_e$  are the electronic charge and mass, respectively, and SW is the total spectral weight of Equation (3), that is,  $\text{SW}_D + \text{SW}_F + \text{SW}_M$ . For the most metallic sample, we obtain  $N_{\text{eff}} \approx 6 \times 10^{21} \text{ cm}^{-3}$ , close to the value found in ref. [17] through the analysis of the band structure, while  $N_{\text{eff}} \approx 4.5 \times 10^{21} \text{ cm}^{-3}$

for the sample grown at  $10^{-3}$  mbar. Finally, for the most insulating sample  $N_{\text{eff}} \approx 3 \times 10^{21} \text{ cm}^{-3}$ . The decreasing behavior of  $N_{\text{eff}}$  is fully consistent with the transition from metallic to insulating state.

#### 4. Conclusions

In conclusion, we have reported the successful growth of strontium niobate SrNbO<sub>3</sub> thin films by PLD technique on (110) oriented DyScO<sub>3</sub> substrates. The lattice mismatch between film and substrate (i.e., about -1,5%) was relatively low to allow the fully strained growth of 15 nm-thick films. The oxygen content in the SNO films was varied by tuning the background deposition oxygen pressure. Investigation of the transport properties did not reveal substantial differences between strained films on SNO and strainless ones, while the overall metallicity is strongly influenced by the oxygen content. The effect of the latter on optical properties was investigated by IR spectroscopy, showing that the SNO films exhibit a metal-to-insulator transition driven by the increase of the oxygen contents. Optical measurements identify three major contributions in the optical conductivity, namely a Drude term, a far-IR band and a mid-IR band, whereby the first one disappears in the most oxygenated and insulating sample. This work contributes to elucidate the electronic properties of SNO thin films with optical measurements and indicates SNO as an ideal candidate for multi-layered epitaxial heterostructures exploiting the oxygen-driven MIT transition.

#### 5. Experimental Section

The epitaxial SNO thin films were grown by PLD on single-crystal (110)-oriented DyScO<sub>3</sub> substrates at the in situ NFFA facility, which integrates the APE beamlines at IOM-CNR at Elettra in Trieste.<sup>[38]</sup> Laser pulses produced by a KrF excimer laser source operating at 300 mJ and at a repetition rate of 3 Hz were focused on a polycrystalline SNO target (purity 99.99%) with an energy density of about 2.5 J cm<sup>-2</sup>. The growth processes were performed in an ultra-pure oxygen background atmosphere (i.e., purity 6.0) ranging from 10<sup>-5</sup> to 10<sup>-1</sup> mbar and at about 700 °C and cooled down to room temperature in about 15 min at the same deposition pressure condition. Growth at higher oxygen pressure (i.e., 1 mbar) resulted into polycrystalline/amorphous films with no evidence of structural order at XRD analysis. The SNO films grown at lowest (10<sup>-5</sup> mbar) and highest (10<sup>-1</sup> mbar) oxygen pressure substantially mimic the electronic behavior of samples grown at 10<sup>-4</sup> and 10<sup>-2</sup> mbar, respectively. The authors thus decided to restrict their study on the films grown in oxygen pressure 10<sup>-4</sup> to 10<sup>-2</sup> mbar, since this range is large enough to promote the transition of the films from metallic to insulating. The actual growth rate of the films was estimated ex situ by XRR measurements. For all the films, the typical growth rate was 72 laser shots per unit cell (i.e., 0.33 nm min<sup>-1</sup> for repetition rate of 1 Hz).

Structural characterization was carried out ex situ using a four-circle Panalytical X'pert diffractometer with a Cu K $\alpha$  radiation source. In particular, the high resolution configuration for XRD was achieved by using a 4-bounce (220)-Ge monochromator able to select the K $\alpha_1$  wavelength alone, while high-intensity configuration allowed higher photon flux (i.e., about 2 orders of magnitude), yet allowing both Cu K $\alpha_1$  and K $\alpha_2$  wavelengths.

The structural and morphological high quality of the surface of SNO thin film had been probed in situ by scanning tunneling microscopy (STM) and low energy electron diffraction (LEED) apparatus at the APE-IOM beamline at Elettra synchrotron facility.<sup>[39]</sup> Both STM and LEED investigations were carried out on the freshly grown SNO samples transferred in situ from PLD growth chamber directly under UHV (<10<sup>-10</sup> mbar).

HRTEM experiments were performed using a JEOL 2010 UHR TEM equipped with a field emission gun and operated at 200 kV. Microscopy data analysis was performed with the Gatan Microscopy Suite 3.20.1314.0 (GMS). Cross-sectional HRTEM samples were prepared with a conventional polishing technique followed by dimpling and milling with Ar ions. This preparation procedure had been proved to minimize structural and chemical modifications of cross-sectional TEM samples and had successfully been applied to other oxide thin-film systems.<sup>[40–42]</sup>

Infrared reflectance measurements at room temperature were performed at the SISSI-Material Science branchline at Elettra synchrotron in Trieste by means of FTIR spectroscopy with an infrared microscope Bruker Hyperion 2000 coupled with a Michelson interferometer Bruker Vertex 70v.<sup>[43]</sup> By changing the internal source, the beam-splitter, and the detector in the experimental set-up, the authors were able to cover the infrared spectral range of 70–8000 cm<sup>-1</sup>, that is ≈ 0.009–1 eV.

Density functional theory (DFT) calculations were performed at the CNR-ISMN high-performance computing facility using the Quantum Espresso program package.<sup>[44,45]</sup> The calculations were performed by applying the Perdew–Burke–Ernzerhof parametrization<sup>[46]</sup> of the generalized gradient approximation. Electronic states were described by using scalar-relativistic optimized norm-conserving Vanderbilt pseudopotentials<sup>[47]</sup> and wavefunctions expanded plane-wave basis set with a cutoff of 50 Ry. The Brillouin zone was sampled by using a *k*-point mesh grid of 11 × 11 × 11 points. This set-up was consistent with the conditions adopted in previous works focused on the evaluation of the dielectric properties of Sr and Nb oxides.<sup>[48]</sup> The complex dielectric tensor was obtained from the DFT eigenvalues and eigenvectors calculated in the random phase approximation.<sup>[49]</sup> In the calculation of the optical conductivity, a Lorentzian broadening of 2.0 and 0.2 eV was used for inter-band and metal Drude-like terms, respectively.

## Acknowledgements

This work has been partially performed in the framework of the Nanoscience Foundry and Fine Analysis (NFFA-MIUR Italy Progetti Internazionali) facility.

Open access Funding provided by Consiglio Nazionale delle Ricerche within the CRUI-CARE Agreement.

## Conflict of Interest

The authors declare no conflict of interest.

## Data Availability Statement

The data that support the findings of this study are available from the corresponding author upon reasonable request.

## Keywords

high-resolution transmission electron microscopy, infrared spectroscopy, perovskite oxides, thin-films, X-ray powder diffraction

Received: December 8, 2021

Revised: February 3, 2022

Published online:

- [3] M. Coll, J. Fontcuberta, M. Althammer, M. Bibes, H. Boschker, A. Calleja, G. Cheng, M. Cuoco, R. Dittmann, B. Dkhil, I. El Baggari, M. Fanciulli, I. Fina, E. Fortunato, C. Frontera, S. Fujita, V. Garcia, S. Goennenwein, C.-G. Granqvist, J. Grollier, R. Gross, A. Hagfeldt, G. Herranz, K. Hono, E. Houwman, M. Huijben, A. Kalaboukhov, D. Keeble, G. Koster, L. Kourkoutis, et al., *Appl. Surf. Sci.* **2019**, *482*, 1.
- [4] Q. Ji, L. Bi, J. Zhang, H. Cao, X. S. Zhao, *Energy Environ. Sci.* **2020**, *13*, 1408.
- [5] P. Scheiderer, M. Schmitt, J. Gabel, M. Zapf, M. Stübinger, P. Schütz, L. Dudy, C. Schlueter, T.-L. Lee, M. Sing, R. Claessen, *Adv. Mater.* **2018**, *30*, 1706708.
- [6] A. Herpers, C. Lenser, C. Park, F. Offi, F. Borgatti, G. Panaccione, S. Menzel, R. Waser, R. Dittmann, *Adv. Mater.* **2014**, *26*, 2730.
- [7] F. Borgatti, C. Park, A. Herpers, F. Offi, R. Egoavil, Y. Yamashita, A. Yang, M. Kobata, K. Kobayashi, J. Verbeeck, G. Panaccione, R. Dittmann, *Nanoscale* **2013**, *5*, 3954.
- [8] X. Xu, C. Randorn, P. Efstathiou, J. T. Irvine, *Nat. Mater.* **2012**, *11*, 595.
- [9] D. Y. Wan, Y. L. Zhao, Y. Cai, T. C. Asmara, Z. Huang, J. Q. Chen, J. Hong, S. M. Yin, C. T. Nelson, M. R. Motapohtula, B. X. Yan, D. Xiang, X. Chi, H. Zheng, W. Chen, R. Xu, Ariando, A. Rusydi, A. M. Minor, M. B. H. Breese, M. Sherburne, M. Asta, Q.-H. Xu, T. Venkatesan, *Nat. Commun.* **2017**, *8*, 15070.
- [10] T. C. Asmara, D. Wan, Y. Zhao, M. A. Majidi, C. T. Nelson, M. C. Scott, Y. Cai, B. Yan, D. Schmidt, M. Yang, T. Zhu, P. E. Trevisanutto, M. R. Motapohtula, Y. P. Feng, M. B. H. Breese, M. Sherburne, M. Asta, A. Minor, T. Venkatesan, A. Rusydi, *Nat. Commun.* **2017**, *8*, 15271.
- [11] D. Oka, Y. Hirose, S. Nakao, T. Fukumura, T. Hasegawa, *Phys. Rev. B* **2015**, *92*, 205102.
- [12] Y. Park, J. Roth, D. Oka, Y. Hirose, T. Hasegawa, A. Paul, A. Pogrebnnyakov, V. Gopalan, T. Birol, R. Engel-Herbert, *Commun. Phys.* **2020**, *3*, 102.
- [13] M. Mirjoleit, M. Kataja, T. K. Hakala, P. Komissinskiy, L. Alff, G. Herranz, J. Fontcuberta, *Adv. Opt. Mater.* **2021**, *9*, 2100520.
- [14] R. Uecker, R. Bertram, M. Brützmam, Z. Galazka, T. M. Gesing, C. Guguschev, D. Klimm, M. Klupsch, A. Kwasniewski, D. G. Schlom, *J. Cryst. Growth* **2017**, *457*, 137.
- [15] G. Koster, L. Klein, W. Siemons, G. Rijnders, J. S. Dodge, C.-B. Eom, D. H. A. Blank, M. R. Beasley, *Rev. Mod. Phys.* **2012**, *84*, 253.
- [16] A. Nardi, C. Bigi, S. Kumar Chaluvadi, R. Ciancio, J. Fujii, I. Vobornik, G. Panaccione, G. Rossi, P. Orgiani, *Coatings* **2020**, *10*, 780.
- [17] C. Bigi, P. Orgiani, J. Sławińska, J. Fujii, J. T. Irvine, S. Picozzi, G. Panaccione, I. Vobornik, G. Rossi, D. Payne, F. Borgatti, *Phys. Rev. Mater.* **2020**, *4*, 025006.
- [18] H. Hannerz, G. Svensson, S. Y. Istomin, O. G. D'Yachenko, *J. Solid State Chem.* **1999**, *147*, 421.
- [19] K. Balasubramaniam, Y. Cao, N. Patel, S. Havelia, P. Cox, E. Devlin, E. Yu, B. Close, P. Woodward, P. Salvador, *J. Solid State Chem.* **2008**, *181*, 705.
- [20] D. P. Norton, *Mater. Sci. Eng., R* **2004**, *43*, 139.
- [21] D. G. Schlom, L.-Q. Chen, X. Pan, A. Schmehl, M. A. Zurbuchen, *J. Am. Ceram. Soc.* **2008**, *91*, 2429.
- [22] P. Orgiani, A. Y. Petrov, R. Ciancio, A. Galdi, L. Maritato, B. A. Davidson, *Appl. Phys. Lett.* **2012**, *100*, 042404.
- [23] H. Y. Hwang, S. W. Cheong, P. G. Radaelli, M. Marezio, B. Batlogg, *Phys. Rev. Lett.* **1995**, *75*, 914.
- [24] X. Zhong-tang, J. Kui-juan, G. Lin, J. Yu-ling, G. Chen, W. Can, G. Hai-zhong, L. Hui-bin, Z. Rui-qiang, Y. Guo-zhen, *Small* **2012**, *8*, 1279.
- [25] H. Cai, X. Wu, J. Gao, *Chem. Phys. Lett.* **2009**, *467*, 313.
- [26] Y.-Q. Xu, S.-Y. Wu, J.-X. Guo, L.-N. Wu, L. Peng, *J. Phys. Chem. Solids* **2017**, *111*, 403.
- [27] P. Orgiani, A. Perucchi, D. Knez, R. Ciancio, C. Bigi, S. K. Chaluvadi, J. Fujii, I. Vobornik, G. Panaccione, G. Rossi, S. Lupi, P. Di Pietro, *Phys. Rev. Appl.* **2020**, *13*, 044011.

[1] J. Mannhart, D. G. Schlom, *Science* **2010**, *327*, 1607.

[2] Y. Tokura, M. Kawasaki, N. Nagaosa, *Nat. Phys.* **2017**, *13*, 1056.

- [28] H. M. I. Jaim, S. Lee, X. Zhang, I. Takeuchi, *Appl. Phys. Lett.* **2017**, *111*, 172102.
- [29] M. Tyunina, L. L. Rusevich, E. A. Kotomin, O. Pacheroova, T. Kocourek, A. Dejneka, *J. Mater. Chem. C* **2021**, *9*, 1693.
- [30] D. L. Windt, *Comput. Phys.* **1998**, *12*, 360.
- [31] M. S. del Rio, R. J. Dejus, in *Proc. SPIE 8141* (Eds: M. S. delRio, O. Chubar), International Society for Optics and Photonics, SPIE **2011**, 368.
- [32] A. Kuzmenko, *Rev. Sci. Instrum.* **2005**, *76*, 083108.
- [33] L. Baldassarre, A. Perucchi, S. Lupi, P. Dore, *J. Phys. Condens. Matter* **2010**, *22*, 355402.
- [34] P. Di Pietro, J. Hoffman, A. Bhattacharya, S. Lupi, A. Perucchi, *Phys. Rev. Lett.* **2015**, *114*, 156801.
- [35] I. L. Vecchio, A. Perucchi, P. Di Pietro, O. Limaj, U. Schade, Y. Sun, M. Arai, K. Yamaura, S. Lupi, *Sci. Rep.* **2013**, *3*, 2990.
- [36] L. Baldassarre, A. Perucchi, E. Arcangeletti, D. Nicoletti, D. Di Castro, P. Postorino, V. A. Sidorov, S. Lupi, *Phys. Rev. B: Condens. Matter Mater. Phys.* **2007**, *75*, 245108.
- [37] S. Lupi, M. Ortolani, P. Calvani, *Phys. Rev. B* **2004**, *69*, 180506.
- [38] NFFA, Nanoscience Foundries and Fine Analysis (NFFA) - Trieste, <https://www.trieste.nffa.eu/> (accessed: April 2017).
- [39] G. Panaccione, I. Vobornik, J. Fujii, D. Krizmancic, E. Annese, L. Giovanelli, F. Maccherozzi, F. Salvador, A. De Luisa, D. Benedetti, A. Gruden, P. Bertoch, F. Polack, D. Cocco, G. Sostero, B. Diviacco, M. Hochstrasser, U. Maier, D. Pescia, C. H. Back, T. Greber, J. Osterwalder, M. Galaktionov, M. Sancrotti, G. Rossi, *Rev. Sci. Instrum.* **2009**, *80*, 043105.
- [40] D. Knez, G. Dražić, S. K. Chaluvadi, P. Orgiani, S. Fabris, G. Panaccione, G. Rossi, R. Ciancio, *Nano Lett.* **2020**, *20*, 6444.
- [41] P. Rajak, D. Knez, S. K. Chaluvadi, P. Orgiani, G. Rossi, L. Méchin, R. Ciancio, *ACS Appl. Mater. Interfaces* **2021**, *13*, 55666.
- [42] R. Ciancio, E. Carlino, C. Aruta, D. Maccariello, F. M. Granozio, U. Scotti di Uccio, *Nanoscale* **2012**, *4*, 91.
- [43] S. Lupi, A. Nucara, A. Perucchi, P. Calvani, M. Ortolani, L. Quaroni, M. Kiskinova, *J. Opt. Soc. Am. B* **2007**, *24*, 959.
- [44] P. Giannozzi, S. Baroni, N. Bonini, M. Calandra, R. Car, C. Cavazzoni, D. Ceresoli, G. L. Chiarotti, M. Cococcioni, I. Dabo, A. Dal Corso, S. de Gironcoli, S. Fabris, G. Fratesi, R. Gebauer, U. Gerstmann, C. Gougoussis, A. Kokalj, M. Lazzeri, L. Martin-Samos, N. Marzari, F. Mauri, R. Mazzarello, S. Paolini, A. Pasquarello, L. Paulatto, C. Sbraccia, S. Scandolo, G. Sclauzero, A. P. Seitsonen, et al., *J. Phys. Condens. Matter* **2009**, *21*, 395502.
- [45] P. Giannozzi, O. Andreussi, T. Brumme, O. Bunau, M. B. Nardelli, M. Calandra, R. Car, C. Cavazzoni, D. Ceresoli, M. Cococcioni, N. Colonna, I. Carnimeo, A. D. Corso, S. de Gironcoli, P. Delugas, R. A. D. Jr, A. Ferretti, A. Floris, G. Fratesi, G. Fugallo, R. Gebauer, U. Gerstmann, F. Giustino, T. Gorni, J. Jia, M. Kawamura, H.-Y. Ko, A. Kokalj, E. Küçükbenli, M. Lazzeri, et al., *J. Phys. Condens. Matter* **2017**, *29*, 465901.
- [46] J. P. Perdew, K. Burke, M. Ernzerhof, *Phys. Rev. Lett.* **1996**, *77*, 3865.
- [47] M. Schlipf, F. Gygi, *Comput. Phys. Commun.* **2015**, *196*, 36.
- [48] G. Parusa, A. Syahroni, M. A. Majidi, *IOP Conf. Ser.: Mater. Sci. Eng.* **2020**, *902*, 012059.
- [49] D. Bohm, D. Pines, *Phys. Rev.* **1953**, *92*, 609.